

## Article

# One Step Synthesis of Oxygen Defective Bi@Ba<sub>2</sub>TiO<sub>4</sub>/BaBi<sub>4</sub>Ti<sub>4</sub>O<sub>15</sub> Microsheet with Efficient Photocatalytic Activity for NO Removal

Ting Gao <sup>1</sup>, Ke Zhang <sup>1,\*</sup>, Qihui Zhu <sup>1</sup>, Qingyun Tian <sup>1</sup>, Hui Wang <sup>1</sup>, Wei Zhang <sup>1</sup>, Jiangyushan Liang <sup>1</sup>, Jingqi Lin <sup>1</sup>, Ahmed A. Allam <sup>2</sup>, Jamaan S. Ajarem <sup>3</sup>, Peter K. J. Robertson <sup>4</sup> and Chuanyi Wang <sup>1,\*</sup>

<sup>1</sup> School of Environmental Science and Engineering, Shaanxi University of Science and Technology, Xi'an 710021, China

<sup>2</sup> Zoology Department, Faculty of Science, Beni-Suef University, Beni-Suef 62511, Egypt

<sup>3</sup> Zoology Department, College of Science, King Saud University, Riyadh 11362, Saudi Arabia

<sup>4</sup> School of Chemistry and Chemical Engineering, Queen's University Belfast, Stranmillis Road, Belfast BT9 5AG, UK

\* Correspondence: 4310@sust.edu.cn (K.Z.); wangchuanyi@sust.edu.cn (C.W.)

**Abstract:** Photocatalysis is an effective technology for NO removal even at low concentrations in the ambient atmosphere. However, the low efficiency of this advanced process and the tendency of producing toxic byproducts hinder the practical application of photocatalysis. To overcome these problems, the Bi@Ba<sub>2</sub>TiO<sub>4</sub>/BaBi<sub>4</sub>Ti<sub>4</sub>O<sub>15</sub> photocatalytic composites were successfully prepared by a one-step hydrothermal method. The as-synthesized photocatalysts exhibited an efficient photocatalytic performance and generated low amounts of toxic byproducts. X-ray diffraction studies show that Bi<sup>3+</sup> is successfully reduced on the surface of Ba<sub>2</sub>TiO<sub>4</sub>/BaBi<sub>4</sub>Ti<sub>4</sub>O<sub>15</sub> (BT/BBT). After L-Ascorbic acid (AA) modification, the photocatalytic NO removal efficiency of Bi@Ba<sub>2</sub>TiO<sub>4</sub>/BaBi<sub>4</sub>Ti<sub>4</sub>O<sub>15</sub> is increased from 25.55% to 67.88%, while the production of the toxic byproduct NO<sub>2</sub> is reduced by 92.02%, where the initial concentration of NO is diluted to ca. 800 ppb by the gas stream and the flow rate is controlled at 301.98 mL·min<sup>-1</sup> in a 150 mL cylindrical reactor. Furthermore, ambient humidity has little effect on the photocatalytic performance of the Bi@Ba<sub>2</sub>TiO<sub>4</sub>/BaBi<sub>4</sub>Ti<sub>4</sub>O<sub>15</sub>, and the photocatalyst exhibits excellent reusability after repeated cleaning with deionized water. The improved photocatalytic effect is attributed to the addition of AA in BT/BBT being able to reduce Bi<sup>3+</sup> ions to form Bi nanoparticles giving surface plasmon effect (SPR) and generate oxygen vacancies (OVs) at the same time, thereby improving the separation efficiency of photogenerated carriers, enhancing the light absorption, and increasing the specific surface areas. The present work could provide new insights into the design of high-performance photocatalysts and their potential applications in air purification, especially for NO removal.

**Keywords:** photocatalysis; BaBi<sub>4</sub>Ti<sub>4</sub>O<sub>15</sub>; surface plasmon effect; NO removal



**Citation:** Gao, T.; Zhang, K.; Zhu, Q.; Tian, Q.; Wang, H.; Zhang, W.; Liang, J.; Lin, J.; Allam, A.A.; Ajarem, J.S.; et al. One Step Synthesis of Oxygen Defective Bi@Ba<sub>2</sub>TiO<sub>4</sub>/BaBi<sub>4</sub>Ti<sub>4</sub>O<sub>15</sub> Microsheet with Efficient Photocatalytic Activity for NO Removal. *Catalysts* **2022**, *12*, 1455. <https://doi.org/10.3390/catal12111455>

Academic Editor: Leonarda Liotta

Received: 12 October 2022

Accepted: 15 November 2022

Published: 17 November 2022

**Publisher's Note:** MDPI stays neutral with regard to jurisdictional claims in published maps and institutional affiliations.



**Copyright:** © 2022 by the authors. Licensee MDPI, Basel, Switzerland. This article is an open access article distributed under the terms and conditions of the Creative Commons Attribution (CC BY) license (<https://creativecommons.org/licenses/by/4.0/>).

## 1. Introduction

With rapid global industrialization, air contamination is becoming an increasingly serious environmental problem. Nitrogen oxide (NO<sub>x</sub>) pollution is one kind of highly dangerous atmospheric pollutant, because it not only promotes the occurrence of photochemical smog but also increases the exposure degree of acid rain for humans and animals [1]. Generally, traditional methods to reduce NO<sub>x</sub> emissions include biochemical reactive filtration, physical adsorption, and biocatalytic oxidation/reduction, but these techniques are very inefficient at low concentration (ppb) level [2]. Photocatalysis is considered an exciting method for NO<sub>x</sub> removal at ppb level in the atmosphere, due to the advantages of this advanced process being energy-saving, environmentally friendly, and sustainable [3–5]. During the photocatalytic process of NO removal, there are, however, various problems

at present, including low activity, unstable effects, and easy to produce toxic byproducts ( $\text{NO}_2$ ). Therefore, it is necessary to develop new photocatalytic semiconductor materials to resolve these issues.

Two-dimension materials have rich catalytic active sites, due to their large contact surface areas and short charge transport paths, such as graphene, transition metal oxides, transition metal dichalcogenides, and nitrides [6,7]. Bismuth-based two-dimensional perovskite  $\text{BaBi}_4\text{Ti}_4\text{O}_{15}$  (BBT) is one of the novel transition metal oxides for reducing  $\text{NO}_x$  emissions. BBT consists of  $(\text{Bi}_2\text{O}_2)^{2+}$  layers interleaved with perovskite-like  $(\text{BaBi}_2\text{Ti}_4\text{O}_{13})^{2-}$ , which has excellent stability. BBT promotes photogenerated charge separation and minimizes their recombination because its obvious internal polarization leads to an outstanding photocatalytic activity under ultraviolet light [8,9]. In addition, the near-ultraviolet spectrum region is 200–400 nm, but more than 50% of solar energy lies within the visible spectral range (400–750 nm) [10]. The  $\text{BaBi}_4\text{Ti}_4\text{O}_{15}$  has a poor absorption of visible light, resulting in unsatisfactory photocatalytic performance under visible light irradiation. Previously, many methods have been developed to enhance the visible light activity of photocatalysts, including metal loading, introduction of vacancies, and heterostructure construction [11–14]. Extensive studies on supported single-atom catalysts (SACs) for photocatalysis have been conducted aiming to achieve interesting properties like high activity, selectivity, and maximum atomic utilization [15]. Altass et al. [16] reported that modification with an appropriate amount of palladium (Pd) nanoparticles enhanced the activity of CO oxidation over the reduced graphene oxide/copper metal organic framework nanocomposite. Furthermore, the introduction of plasmonic metals into photocatalysts is an effective way to extend the light absorption range [17–19]. For example, Duan et al. [20] studied plasmonic Ag on  $\text{TiO}_2$  nanocomposites for photocatalytic NO removal under visible light and found that the surface plasmon resonance (SPR) effect of Ag is responsible for the improvement of the visible-light photoactivity. They also discovered that a very limited loading amount (about 0.89% in Ag/Ti molar ratio) of Ag in  $\text{TiO}_2$  can remarkably improve the photocatalytic activity of NO removal [21]. By studying cesium ferrite nanocomposites decorated with gold selenide quantum dots ( $\text{AuSe}/\text{Cs}_2\text{Fe}_2\text{O}_4$  NC), Alshorifi et al. [22] discovered that metal particle size is one of the most important factors affecting the SPR energy band. However, these noble metals are expensive and unsuitable for industrial applications. Hence, the development of less expensive plasmonic metals is highly desired. Recently, the SPR effect has been found on the cheaper metallic bismuth ( $\text{Bi}^0$ ), which allows hot carriers to be transferred from Bi to the semiconductor. Simultaneously, the introduction of vacancies to photocatalysts is a prospective strategy to tune the surface electronic energy state, which could adjust the reaction pathway and inhibit the formation of toxic by-products [23]. Due to its eco-friendly attributes and excellent biocompatibility, ascorbic acid (AA) is regarded as a suitable reducing agent. Since photogenerated electrons and holes could be separated into two distinct parts in heterojunction composites, creating heterojunction composites with appropriate structures is a promising method to reduce photogenerated carrier recombination [24]. Therefore, it is expected that the coupling of  $\text{Bi}^0$ , oxygen vacancies (OVs) and heterojunction on  $\text{BaBi}_4\text{Ti}_4\text{O}_{15}$  has a conspicuous potential for improving photocatalytic performance for NO removal.

Herein, a one-step hydrothermal method for the synthesis of  $\text{Bi}@\text{Ba}_2\text{TiO}_4/\text{BaBi}_4\text{Ti}_4\text{O}_{15}$  microsheets photocatalyst with OVs and Bi SPR effect is reported. The effect of microtopography, the concentration of Bi, optical properties, atmosphere humidity, and NO conversion mechanism are discussed. The synthesized photocatalyst exhibits high photocatalytic activity with 67.88% of NO converted in 30 min under visible light irradiation, while the  $\text{Bi}@\text{Ba}_2\text{TiO}_4/\text{BaBi}_4\text{Ti}_4\text{O}_{15}$  microsheet produces 92% less byproduct  $\text{NO}_2$  than its counterpart  $\text{Ba}_2\text{TiO}_4/\text{BaBi}_4\text{Ti}_4\text{O}_{15}$  during the photocatalytic process. Furthermore, ambient humidity has little effect on the photocatalytic performance of the  $\text{Bi}@\text{Ba}_2\text{TiO}_4/\text{BaBi}_4\text{Ti}_4\text{O}_{15}$ , and the photocatalyst exhibits excellent reusability after repeated cleaning with deionized water. The good humidity adaptability and remarkable reusability benefit its practical application in photocatalytic NO removal. The detailed mechanism is unveiled by diffused

reflection Fourier transform infrared spectroscopy (DRIFTS), radical trapping, and EPR analyses. Additionally, in the dark, NO could be catalyzed to form  $\text{NO}_3^-$  to a certain extent on the surface of the  $\text{Bi@Ba}_2\text{TiO}_4/\text{BaBi}_4\text{Ti}_4\text{O}_{15}$  microsheet accounting for its specific physicochemical properties. To the best of our knowledge, our study presents the application of  $\text{Bi@Ba}_2\text{TiO}_4/\text{BaBi}_4\text{Ti}_4\text{O}_{15}$  photocatalysts for NO conversion under visible light illumination for the first time.

## 2. Results and Discussion

### 2.1. Photocatalytic Activity

The photocatalytic activities of the as-prepared samples were evaluated for NO removal under visible light irradiation ( $\lambda \geq 420$  nm). Following dark adsorption equilibrium, the NO content was steady when illuminated by visible light. The photocatalytic conversion efficiency curves of various catalysts for NO under visible illumination are compared in Figure 1a. It can be seen that BT/BBT exhibited poor photocatalytic activity with a NO removal efficiency of 25.55%, and this declined over time, which may be a consequence to its unstable nature. The NO elimination efficiency of BT/BBT-0.2 is 47.88%, and the photocatalytic activity trend is increasing initially, then dropping and subsequently gradually increasing finally. BT/BBT-0.1 and BT/BBT-0.05 are found to have NO removal efficiencies of 67.88% and 62.13%, respectively.

According to the aforementioned findings, adding AA significantly affects the catalytic activity of BT/BBT. We speculate that the addition of AA to BT/BBT causes the reduction of Bi ions to form  $\text{Bi}^0$ , which could lead to the SPR effect, as well as creating OVs, thus increasing the content of active sites and specific surface areas in BT/BBT. The best photocatalytic activity requires an optimal AA ratio. The OVs and the SPR effect of  $\text{Bi}^0$  could enhance the light absorption capacity and separation efficiency of the photogenerated carriers, thereby improving its photocatalytic activity.

It is common knowledge that  $\text{NO}_2$ , one of the hazardous byproducts of NO removal, is not a desirable substance [25]. As a result, during the experiments, it is essential to monitor the  $\text{NO}_2$  generation over the various photocatalysts. After 30 min of exposure to visible light, the  $\text{NO}_2$  concentration produced for the BT/BBT-0.05, BT/BBT-0.1, and BT/BBT-0.2 composites are 89.81%, 92.02%, and 86.91% lower than that of obtained when using BT/BBT, respectively (Figure 1b). Furthermore, this indicates that BT/BBT-0.1 is the most advantageous for converting NO into nitrate ions, achieving effective NO removal, and reducing the generation of  $\text{NO}_2$  as an undesirable byproduct.

In general, the photocatalytic activity and stability of the photocatalyst are vital to practical applications. It is observed that during the cyclic photocatalytic NO removal process (Figure 1c), the BT/BBT-0.1 shows a decreased photocatalytic activity (24.71% reduction) after the ten cycles due to the coverage of the surface-active sites by produced nitrate ions. To regenerate the photocatalytic activity, after cyclic testing, the samples were repeatedly washed with deionized water to remove  $\text{NO}_3^-$  from the sample surface. After being rinsed with water, as shown in Figure 1c, the BT/BBT-0.1 recovers its photocatalytic activity (reaching 64.17% NO removal efficiency). These findings suggest that BT/BBT-0.1 has good reusability, and that when the photocatalytic activity is reduced, it can be restored by rinsing with water.

Real-life  $\text{NO}_x$  removal cannot ignore the impact of atmosphere humidity; hence, the effect of relative humidity (RH) on the photocatalytic effect must be investigated. The findings of the humidity-influenced experiments are shown in Figure 1d. The photocatalytic activity of BT/BBT-0.1 is consistent with dry airflow in the range of 40% to 80% relative humidity, implying that the NO photocatalytic reaction active site is rarely bound to water molecules in the atmosphere, which could decrease the probability of competitive adsorption between NO and water molecules. Consequently, due to the excellent humidity adaptation, BT/BBT-0.1 can operate normally for photocatalytic NO conversion in a wide range of climatic conditions.

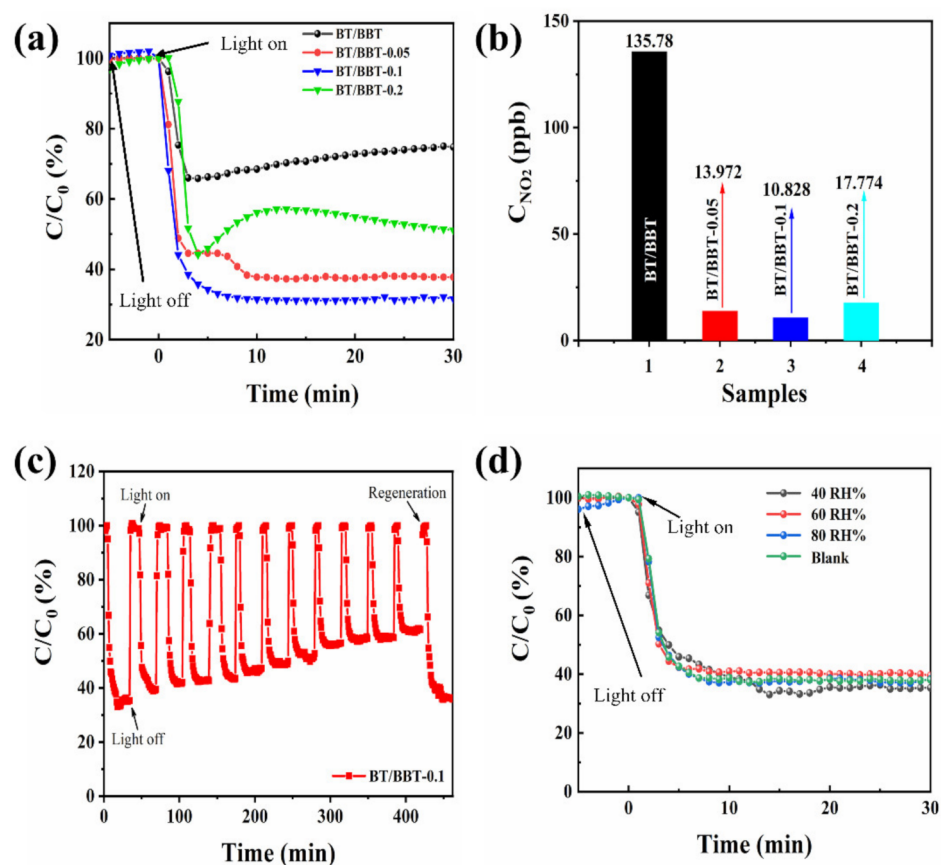


**Figure 1.** (a) Photocatalytic activity of BT/BBT, BT/BBT-0.05, BT/BBT-0.1, and BT/BBT-0.2 under visible light, (b) NO<sub>2</sub> concentration of visible light illumination, (c) ten cycles of photocatalytic activity of BT/BBT-0.1 and the regeneration of photocatalytic activity by rinsed with water, (d) effect of relative humidity on photocatalytic activity of BT/BBT-0.1.

## 2.2. Structural Characterization

The XRD patterns of BT/BBT, BT/BBT-0.05, BT/BBT-0.1, and BT/BBT-0.2 are presented in Figure 2a. The diffraction peaks could be indexed as the Bi, Ba<sub>2</sub>TiO<sub>4</sub> (JCPDS PDF No.38-1481), and BaBi<sub>4</sub>Ti<sub>4</sub>O<sub>15</sub> (JCPDS PDF No.73-2184), which are marked clearly in Figure 2a. The diffraction pattern of BaBi<sub>4</sub>Ti<sub>4</sub>O<sub>15</sub> matches well with the major peaks at  $2\theta = 30.1^\circ$ ,  $32.7^\circ$ ,  $46.9^\circ$ ,  $56.8^\circ$ , which represents the (1 0 9), (1 1 0), (2 0 0), (2 1 9) hkl planes respectively [26]. The secondary phase is similar to orthorhombic Ba<sub>2</sub>TiO<sub>4</sub>. The two strongest secondary phase diffraction peaks appear at  $2\theta = 28.81^\circ$  and  $29.31^\circ$ , which are close to the (2 1 1) and (0 3 1) crystal peaks of the Ba<sub>2</sub>TiO<sub>4</sub> structure [27]. In addition, the two diffraction peaks at  $2\theta = 22.5^\circ$ ,  $27.2^\circ$  could be attributed to metallic Bi reflections, which are connected to the (0 0 3) and (0 1 2) planes [28]. As can be seen, BT/BBT is composed of BaBi<sub>4</sub>Ti<sub>4</sub>O<sub>15</sub> and Ba<sub>2</sub>TiO<sub>4</sub>. Under the same conditions, the intensity of the diffraction peak of Bi monomer (Bi<sup>0</sup>) gradually increases with increasing AA content. When the reducing agent AA content reaches 0.2 g, the intensity of the diffraction peak of Bi<sup>0</sup> exceeds that of BaBi<sub>4</sub>Ti<sub>4</sub>O<sub>15</sub>. This demonstrates that Bi<sup>0</sup> on the surface of the BT/BBT-0.05, BT/BBT-0.1, and BT/BBT-0.10.2 samples are successfully obtained in situ via reduction Bi<sup>3+</sup> ions contained in the BBT samples.

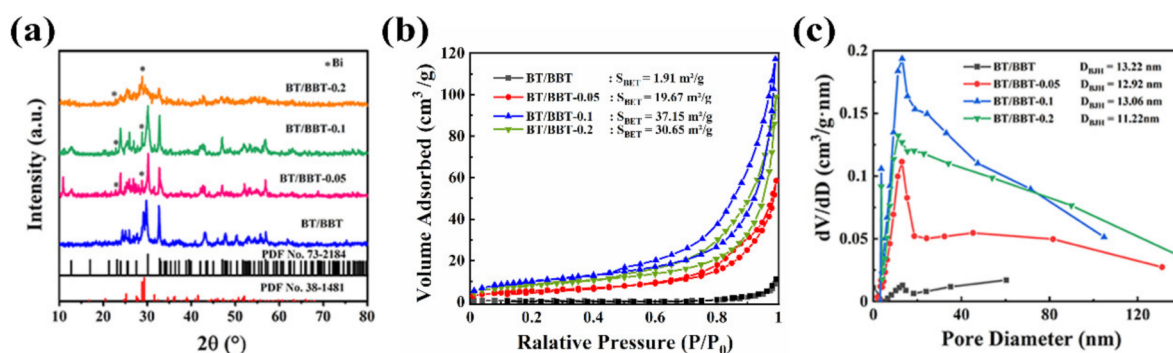


**Figure 2.** (a) XRD patterns, (b) nitrogen adsorption-desorption isotherms, (c) pore size distribution curves of BT/BBT, BT/BBT-0.05, BT/BBT-0.1, and BT/BBT-0.2 composites.

The nitrogen adsorption-desorption isotherms of the obtained samples are displayed in Figure 2b. The specific surface area ( $S_{BET}$ ) of BT/BBT-0.1 hybrids is  $37.15 \text{ m}^2 \text{ g}^{-1}$ , which is the highest among all the samples. The specific surface area ( $S_{BET}$ ) of BT/BBT T/BBT-0.05 and BT/BBT-0.2 composites is found to be  $1.91 \text{ m}^2 \text{ g}^{-1}$ ,  $19.67 \text{ m}^2 \text{ g}^{-1}$ , and  $30.65 \text{ m}^2 \text{ g}^{-1}$  respectively. The  $S_{BET}$  is increased obviously after adding AA, which may be due to the increase in defects that caused structural changes. The pore size distribution curves are shown in Figure 2c, and it can be seen that the maximum diameters ( $D_{BJH}$ ) of all samples are similar (11–14 nm). As a result, the specific surface area of samples is significantly increased by adding the appropriate amount of reducing agent AA, while the pore size is only slightly affected. Despite the fact that all samples have small specific surface areas, their isotherms are identified as type III, and the measured pore sizes are in the mesoporous range (2–50 nm).

As shown in Figure 3, the morphologies of the BT/BBT, BT/BBT-0.05, BT/BBT-0.1, and BT/BBT-0.2 composites were observed by SEM. All the samples are flake-like materials, and BT/BBT-0.1 has the smallest average size ( $d < 0.5 \mu\text{m}$ ). The material's surface becomes rough after the addition of AA, which is consistent with the XRD results. It is common practice to modify materials by adding reducing chemicals, which can modify the morphology of the substance. As shown in Figure S2, the elemental mapping images imply that Bi, Ba, Ti, and O evenly form the BT/BBT-0.1 composite. The EDX analyzer was employed to further verify the element composition and distribution of BT/BBT-0.1. The weight percentages of the Bi, Ba, Ti, and O elements are 67.19, 10.10, 2.47, and 20.23%, respectively.

The optical properties of the samples measured using UV–Vis diffuse reflectance spectroscopy are shown in Figure 4a. As can be seen, BT/BBT microsheets show a clear absorption from the UV to the visible region, with an edge at about 575 nm. In comparison with BT/BBT, increased visible light absorption is achieved by BT/BBT-0.05, BT/BBT-0.1, and BT/BBT-0.2 samples. The widespread absorption is advantageous for the more effective use of solar energy. The significant enhancement of the optical absorption of BT/BBT-0.1 is related to the co-effect of  $\text{Bi}^0$  SPR effect and OVs. The light absorption ability of the samples treated with the reducing agent AA is greatly enhanced due to the generated OVs and SPR effect of  $\text{Bi}^0$  nanoparticles. Moreover, the plots of  $(\alpha h\nu)^{1/2}$  vs. photon energy of samples are displayed in Figure 4b. The band gaps of BT/BBT, BT/BBT-0.05, BT/BBT-0.1, and BT/BBT-0.2 samples are calculated to be 2.88 eV, 2.74 eV, 2.67 eV, and 1.50 eV according to Tauc's equation. These findings suggest that the co-effect of  $\text{Bi}^0$  SPR effect and OVs can boost the intensity of the photocatalyst's response to visible light, facilitating the visible photocatalytic reaction.

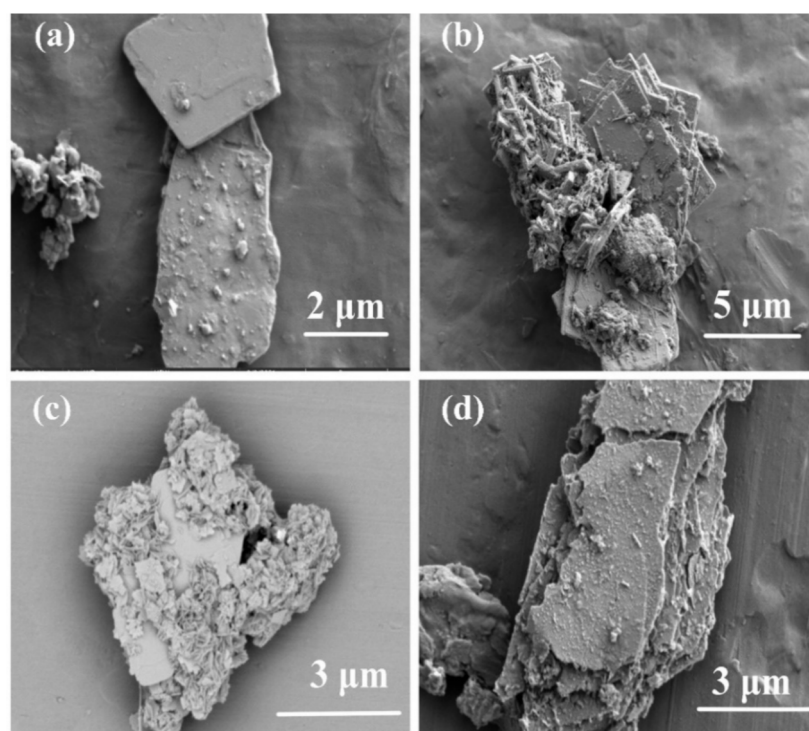


Figure 3. SEM of (a) BT/BBT, (b) BT/BBT-0.05, (c) BT/BBT-0.1, and (d) BT/BBT-0.2.

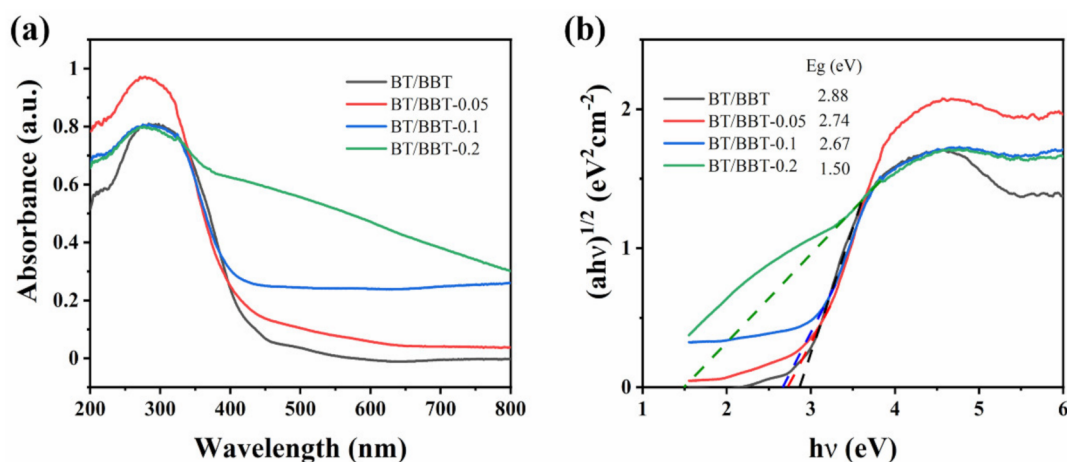
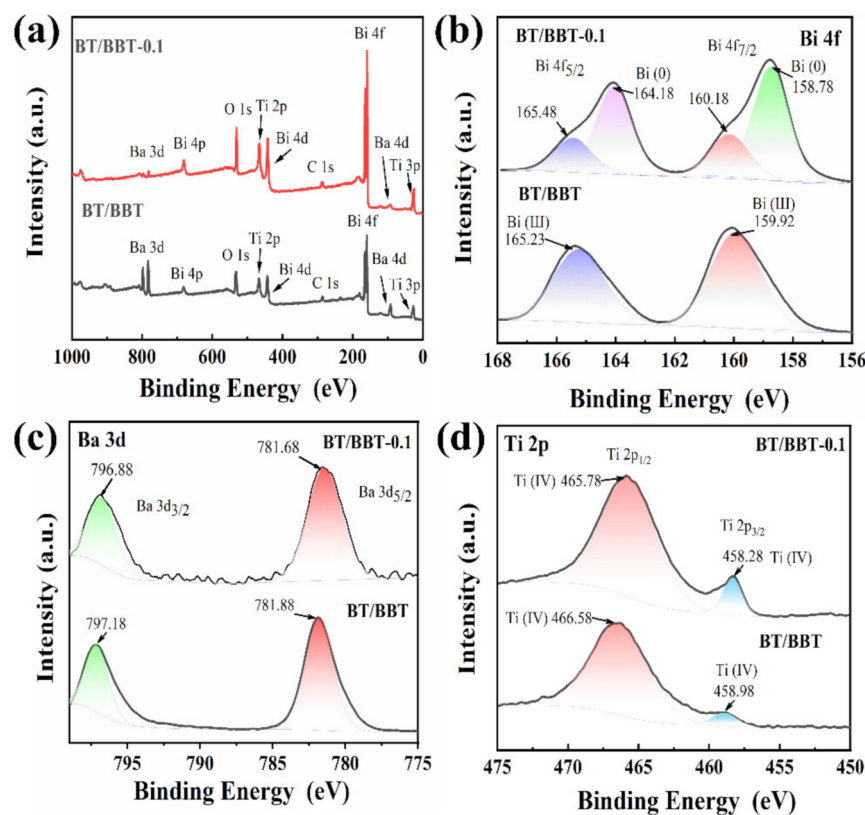


Figure 4. (a) UV-Vis absorption spectra of the sample photocatalysts, (b) plots of  $(\alpha h\nu)^{1/2}$  versus  $h\nu$  of the sample photocatalysts.

As shown in Figure 5, XPS analysis was performed to reveal the chemical states of each element in BT/BBT and BT/BBT-0.1 hybrids. BT/BBT and BT/BBT-0.1 are made up of Ba, Bi, Ti, and O elements. The high-resolution Bi 4f XPS spectrum (Figure 5b) in the BT/BBT and BT/BBT-0.1 shows that the peaks of Bi 4f<sub>7/2</sub> and 4f<sub>5/2</sub> at 160.18 eV and 165.48 eV are the representation of the Bi (III). Moreover, Bi (0) is also observed at 158.78 eV and 164.18 eV in BT/BBT-0.1, indicating that some Bi (III) ions are reduced during the synthesis process [29]. The binding energies of Ba 3d<sub>3/2</sub> and Ba 3d<sub>5/2</sub> are located at 797.18 eV and 781.88 eV in BT/BBT, respectively (Figure 5c) [30], and compared with the peak of Ba in BT/BBT-0.1, the peak of Ba in BT/BBT-0.1 is shifted to lower binding energy (796.88 eV and 781.68 eV). Simultaneously, high-resolution Ti 2p XPS spectra in the BT/BBT shows both the peaks of Ti (IV) at 458.98 eV and 466.58 eV (Figure 5d), whereas the peak shifts to lower binding energy in BT/BBT-0.1 hybrids. The electron binding energy of Ba and

Ti is decreased after the addition of the reducing agent, indicating that electron density is increased, and electron interactions are enhanced [31].



**Figure 5.** XPS spectra of (a) the overall survey, (b) Bi 4f (c) Ba 3d, and (d) Ti 2p on BT/BBT-0.1 and BT/BBT.

The PL emission of photocatalysts is mainly attributed to the recombination of the photoinduced electron and hole. Hence, a lower PL intensity generally reflects a lower recombination rate. The typical PL spectra of BT/BBT, BT/BBT-0.05, BT/BBT-0.1, and BT/BBT-0.2 excited at 534 nm are displayed in Figure 6a. The pristine BT/BBT shows strong emission peaks centered at 580 nm. The PL intensity decreases dramatically as the AA content increasing, and the BT/BBT-0.1 exhibits the lowest PL intensity, which indicates SPR of Bi<sup>0</sup> and OVs suppress recombination of photogenerated charge carriers and thus obtaining higher photocatalytic efficiency.

To further characterize the charge-carrier dynamics during the photocatalytic process, time-resolved fluorescence decay spectra of BT/BBT, BT/BBT-0.05, BT/BBT-0.1, and BT/BBT-0.2 hybrids were recorded. Figure 6b depicts a double exponential decay fitting, with  $\tau_1$  (short lifetime) and  $\tau_2$  (long lifetime). The  $\tau_1$  is attributed to the nonradiative transition and represents the lifetime of excited electrons recombining with surface defects. Meanwhile, the  $\tau_2$  is associated with the inter-band luminescence process and represents the lifetime of excited electrons in CB recombining with holes in VB [32]. The  $\tau_2$  values for photocatalytic samples are associated with the photoexcited electron-hole recombination process, and larger  $\tau_2$  values indicate decreased charge recombination and enhanced charge transfer. Therefore, the generally accepted fluorescence lifetime is the average of the two lifetimes [33]. The results show that BT/BBT-0.1 has a longer carrier lifetime than BT/BBT. A longer fluorescence lifetime of carriers may be responsible for increased photocatalytic activity [34].

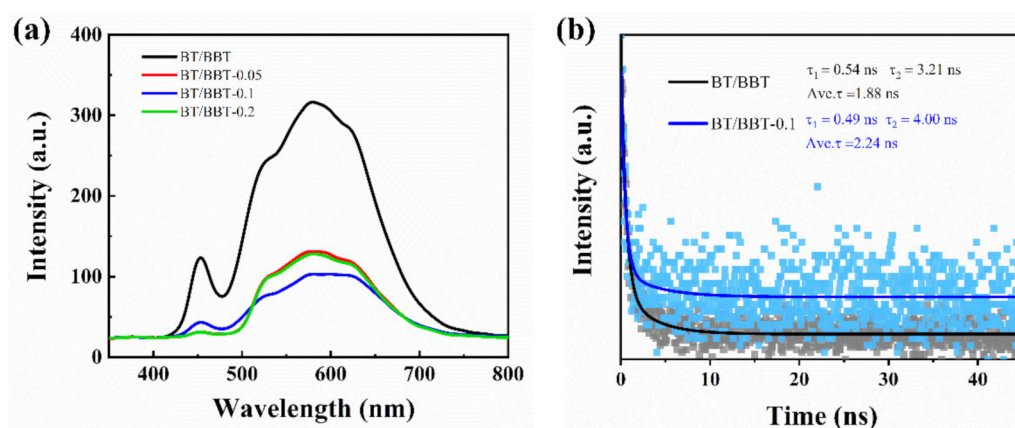


Figure 6. (a) PL spectra, (b) fluorescence lifetime of BT/BBT and BT/BBT-0.1 samples.

The transient photocurrent responses for BT/BBT and BT/BBT-0.1 electrodes under visible light irradiation were measured to gain a better understanding of the behavior of the photoinduced charges (Figure 7a). After loading AA, the corresponding photocurrent increases dramatically, as expected. The increased photocurrent intensity suggests that photoinduced hole–electron pairs are better separated.

The charge transfer process was inspected using EIS in the dark. EIS Nyquist plots of BT/BBT and BT/BBT-0.1 composites are shown in Figure 7b. The arc radius of the BT/BBT-0.1 composite is smaller than that of the BT/BBT composite, indicating a lower charge transfer resistance. These findings support the PL observation, confirming the effective separation and transfer of charge carriers.

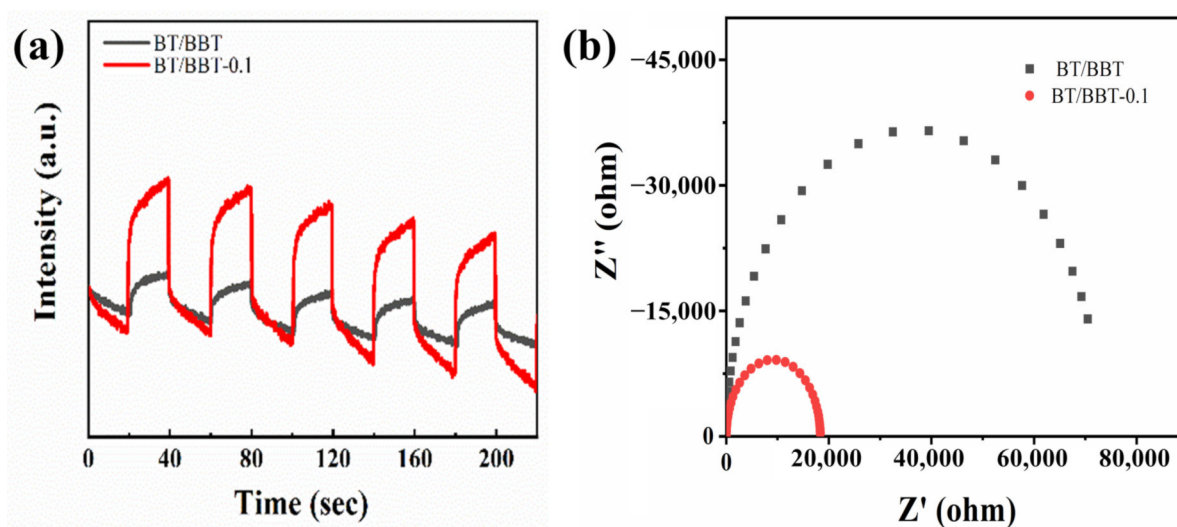
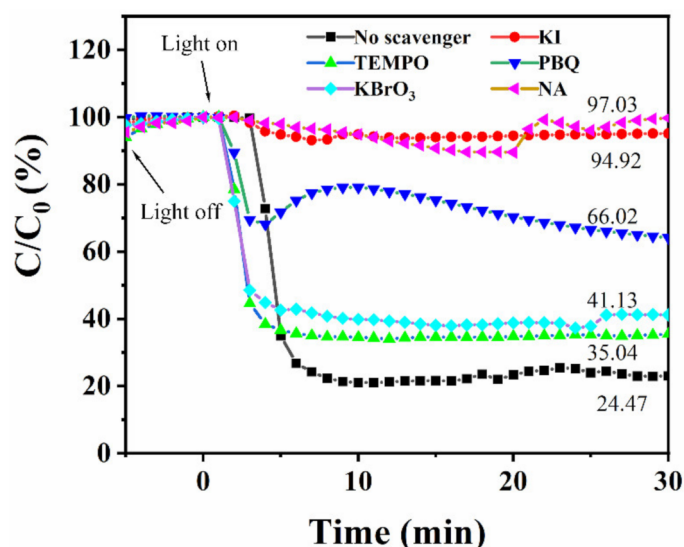


Figure 7. (a) Transient photocurrent responses, (b) EIS spectra of BT/BBT and BT/BBT-0.1 samples.

### 2.3. Photocatalytic Mechanism

To explore the main active substances in the photocatalytic NO conversion reaction, a series of trapping experiments were carried out. PBQ, TEMPO, KBrO<sub>3</sub>, NA, and KI were selected to trap  $\bullet\text{O}_2^-$ ,  $\bullet\text{OH}$ ,  $e^-$ ,  $^1\text{O}_2$ , and  $h^+$ , respectively [35]. As displayed in Figure 8, for BT/BBT-0.1, the addition of KI and NA virtually inhibits the conversion of NO, indicating that light-induced  $h^+$  and  $^1\text{O}_2$  mainly contribute to the photocatalytic NO conversion process. Additionally, when radicals were quenched with PBQ, the conversion efficiency of NO was decreased by approximately 33.98% after 30 min of light irradiation, suggesting that the  $\bullet\text{O}_2^-$  plays a secondary role in the photocatalytic conversion of NO. However, the addition of TEMPO and KBrO<sub>3</sub> does not inhibit the NO removal activity, indicating that  $\bullet\text{OH}$  and  $e^-$  are rarely involved in the NO removal process.

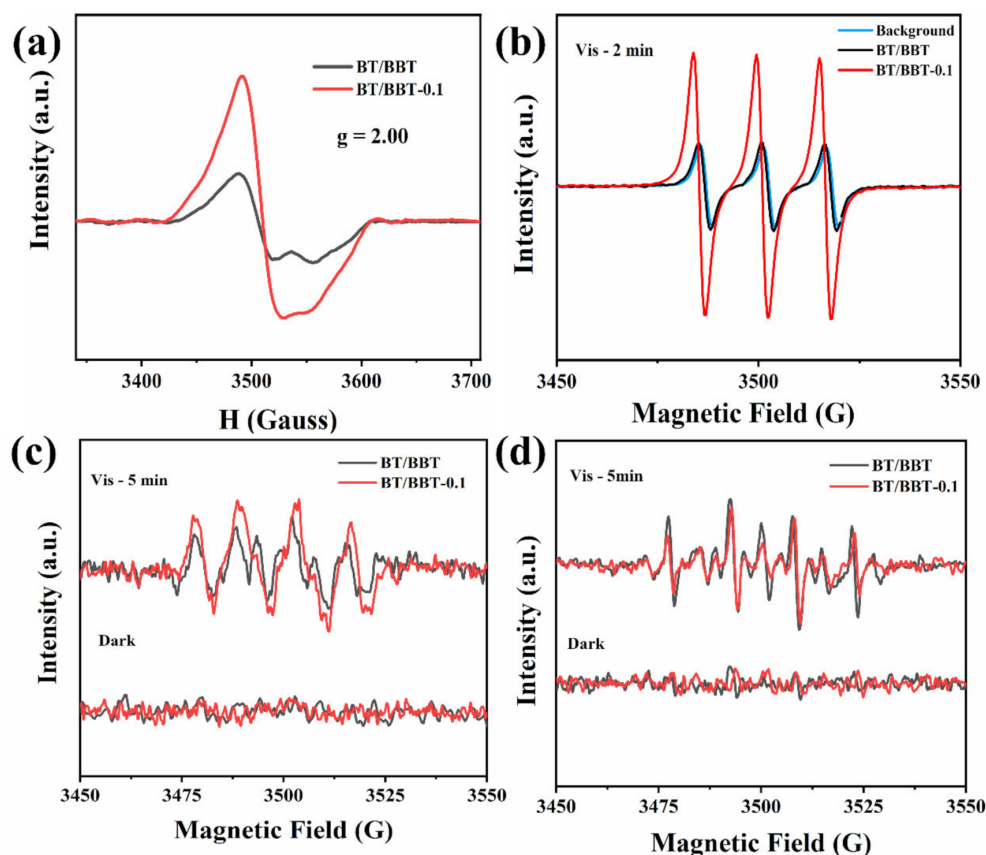


**Figure 8.** Effect of different radical scavengers on NO removal over BT/BBT-0.1.

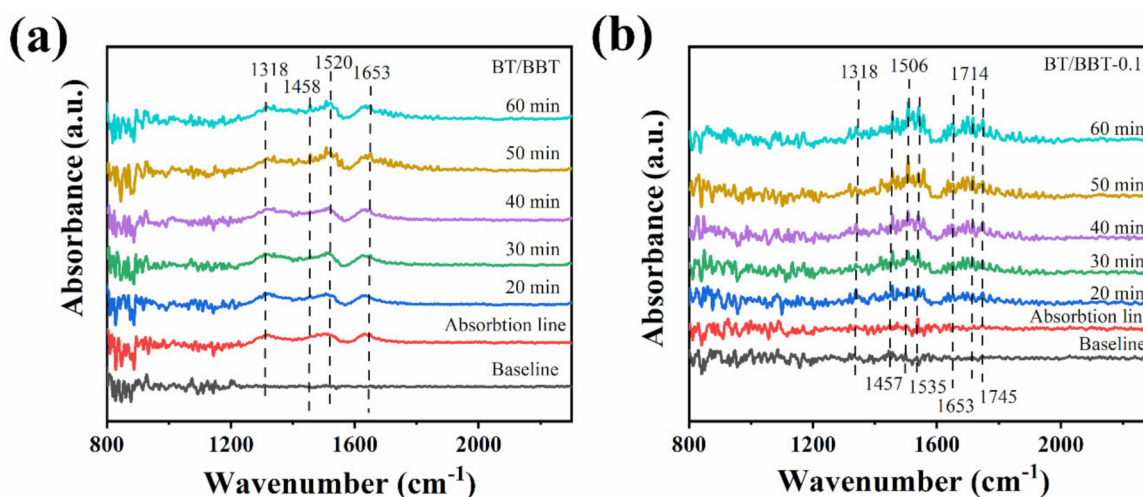
Furthermore, electron spin resonance (ESR) spectroscopy measurement can offer the most persuasive evidence for detecting the reactive species as shown in Figure 9. According to the results, a signal at about  $g = 2.00$  appears, which is assigned to the electrons trapped in OV<sub>s</sub> in BT/BBT and BT/BBT-0.1, and the ESR signal for BT/BBT-0.1 is higher than BT/BBT. This result implies that there are OV<sub>s</sub> in both samples and the number of OV<sub>s</sub> increases in the BT/BBT-0.1. Hence, the OV<sub>s</sub> increasing in BT/BBT-0.1 could be one factor for the enhanced photocatalytic activity because OV<sub>s</sub> promote adsorption of oxygen to form active species such as  $\bullet\text{O}_2^-$  [36]. Under visible light illumination, three characteristic signals of the TEMP- $^1\text{O}_2$  with the nearly relative intensity ratio of 1:1:1 can be observed in Figure 9b. Notably, the signal intensity of BT/BBT-0.1 is higher than that of BT/BBT, implying that BT/BBT-0.1 has a higher concentration of singlet oxygen ( $^1\text{O}_2$ ). Experimental results show that no signal peak arises in neither BT/BBT nor in BT/BBT-0.1 under dark conditions. When exposed to visible light, DMPO- $\bullet\text{O}_2^-$  immediately displays four obvious wave signals with a similar relative intensity ratio of 1:1:1:1 (Figure 9c). Interestingly, under the same illumination time, the peak strength of  $\bullet\text{O}_2^-$  of BT/BBT-0.1 is higher than that of BT/BBT, which is ascribed to the higher free electron concentration of BT/BBT-0.1, so the formation rate of  $\bullet\text{O}_2^-$  is accelerated. Meanwhile, the ESR signal intensities of DMPO- $\bullet\text{OH}$  are close, with a similar relative intensity ratio of 1:2:2:1 (Figure 9d). The above results further confirm the existence of OV<sub>s</sub>,  $^1\text{O}_2$ ,  $\bullet\text{OH}$ , and  $\bullet\text{O}_2^-$ .

In this work, the reaction routes of NO removal were studied by in situ DRIF (Figure 10). The baseline spectra were first recorded before introducing NO and dry clean air into the reaction cell. During the photocatalytic process of BT/BBT, four peaks are observed, as shown in Figure 10a. The peaks of  $\text{NO}_3^-$  at 1520 and 1653  $\text{cm}^{-1}$  suggest that NO is mostly oxidized during the photocatalytic process [37,38]. The absorption bands at 1318  $\text{cm}^{-1}$  are due to  $\text{N}_2\text{O}_4$ , which is the polymerization product of  $\text{NO}_2$  on the surface of BT/BBT [39]. The peak of 1458  $\text{cm}^{-1}$  is attributed to  $\text{NO}_2^-$  [40]. These peaks appear after 30 min of dark adsorption equilibrium and are increased after light irradiation. The result shows that BT/BBT occurs oxidation during the dark adsorption phase, while a larger amount of harmful by-product  $\text{NO}_2$  is formed. In the case of BT/BBT-0.1, as shown in Figure 10b, the infrared absorption peak of  $\text{NO}_x$  on the surface of the photocatalyst is detected. The peaks at 1457, 1506, 1535, and 1653  $\text{cm}^{-1}$  are caused by the  $\text{NO}_3^-$ , and the absorption peak at 1714  $\text{cm}^{-1}$  is due to the nitrosyl [38,39,41]. The absorption peaks at 1318 and 1745  $\text{cm}^{-1}$  are due to the  $\text{N}_2\text{O}_4$  coming from the chelation of  $\text{NO}_2$  [39]. These peaks exhibit a significant increase after visible light irradiation, but do not change significantly during the dark adsorption phase. According to this finding, the catalytic reaction of NO at BT/BBT-0.1

primarily takes place in the light phase and primarily produces  $\text{NO}_3^-$ , with minimal  $\text{NO}_2$  byproduct.

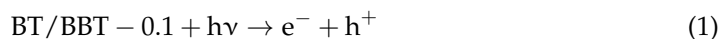


**Figure 9.** (a) ESR spectra of BT/BBT and BT/BBT-0.1; the ESR signals of BT/BBT and BT/BBT-0.1 for (b)  $^1\text{O}_2$ , (c)  $\bullet\text{O}_2^-$  and (d)  $\bullet\text{OH}$  in darkness and under visible light irradiation.



**Figure 10.** In situ DRIFT spectra of adsorption and photocatalytic on (a) BT/BBT and (b) BT/BBT-0.1.

Based on the above results and analysis, a mechanism for NO removal over BT/BBT-0.1 is proposed and illustrated in Figure 11, and the possible photocatalytic reaction is as follows [39,42]:



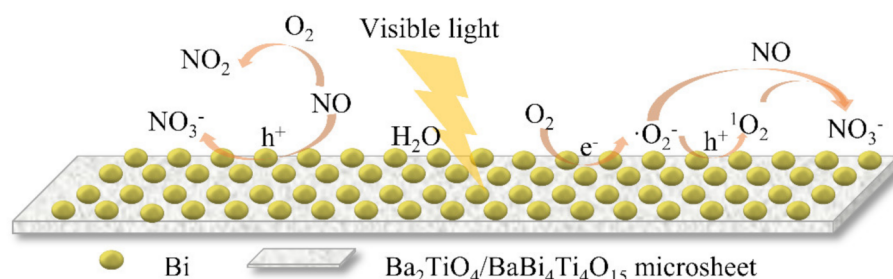
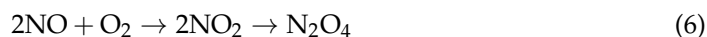


**Figure 11.** Possible reaction mechanism of photocatalytic NO removal over BT/BBT-0.1.

According to the previous analysis, the OV and SPR effect of  $\text{Bi}^0$  play a variety of critical roles in the photocatalytic system. Firstly, the OV and SPR effect of  $\text{Bi}^0$  can increase catalytic reaction activity while inhibiting the formation of  $\text{NO}_2$ . Secondly, the presence of OV and the SPR effect of  $\text{Bi}^0$  can promote light absorption, and effectively separate photogenerated charge carriers. These advantages could lessen ineffective energy loss while promoting light absorption. In addition, the presence of OV and the SPR effect of  $\text{Bi}^0$  promote photocurrent response while decreasing the charge transfer resistance. Lastly, the OV and SPR effect of  $\text{Bi}^0$  can improve the conversion of NO to  $\text{NO}_3^-$  by  $\text{Bi}@\text{Ba}_2\text{TiO}_4/\text{BaBi}_4\text{Ti}_4\text{O}_{15}$  under visible light irradiation.

### 3. Experimental

#### 3.1. Chemicals

$\text{Bi}(\text{NO}_3)_3 \cdot 5\text{H}_2\text{O}$ ,  $\text{BaSO}_4$ ,  $\text{TiO}_2$ ,  $\text{Na}_2\text{SO}_4$ , P-benzoquinone (PBQ), and potassium bromate ( $\text{KBrO}_3$ ) were purchased from Shanghai Macklin Biochemical Co., Ltd, Shanghai, China.  $\text{NaOH}$ , 2,2,6,6-tetramethylpiperidinoxy (TEMPO), 5,5-dimethyl-1-pyrroline N-oxide (DMPO), and L-tryptophan (NA) were obtained from Aladdin Reagent Co., Ltd, Shanghai, China. L-Ascorbic acid (AA) was obtained from Sinopharm Chemical Reagent Co., Ltd. Potassium iodide (KI) was obtained from Shanghai Rhawn Chemical Technology Co. Ltd, Shanghai, China. Anhydrous ethanol was purchased from Tianjin Bohai Chemical Industry Group Co. Ltd, Tianjin, China. All chemicals used in this study are analytical grade without further purification.

#### 3.2. Photocatalyst Preparation

$\text{Ba}_2\text{TiO}_4/\text{BaBi}_4\text{Ti}_4\text{O}_{15}$  powders were synthesized by the hydrothermal method.  $\text{Bi}(\text{NO}_3)_3 \cdot 5\text{H}_2\text{O}$  (4.850 g),  $\text{BaSO}_4$  (0.582 g), and  $\text{TiO}_2$  (0.799 g) were dissolved with vigorous stirring and then mixed with  $3 \text{ mol} \cdot \text{L}^{-1}$   $\text{NaOH}$  solution to adjust the pH value to 12. Then 0.05 g, 0.1 g, and 0.2 g of L-Ascorbic acid (AA) was added to the mixture solution, respectively. This solution was transferred into a polytetrafluoroethylene reaction tank and kept at  $180^\circ\text{C}$  for 9 h. After cooling to room temperature, the sample was washed repeatedly until the filtrate was neutral, and then freeze-dried for 6 h. The obtained samples were named as BT/BBT, BT/BBT-0.05, BT/BBT-0.1, and BT/BBT-0.2, respectively.

#### 3.3. Catalyst Characterization

The crystalline structure of the samples was acquired by X-ray powder diffraction (XRD, D/Max-2200PC, Beijing, China) equipped with Cu K $\alpha$  radiation at 30 kV and 10 mA with a scanning rate of  $16^\circ \text{ min}^{-1}$  in the  $2\theta$  range of  $10^\circ$ – $80^\circ$ .

The optical absorption of the materials over a range of 200–800 nm was determined using ultraviolet-visible light spectroscopy (UV-vis, Shimadzu's UV-1800, Tokyo, Japan)

equipped with an integrating sphere assembly to investigate the optical properties of the samples, using BaSO<sub>4</sub> as the reference.

The morphological surface of samples was investigated by scanning electron microscopy (SEM, FEI's Verios 460, Hillsboro, OR, USA) with a high-resolution field emission. Energy Dispersive X-ray Spectroscopy (EDX) analysis of BT/BBT-0.1 was carried out by the scanning electron microscope (FEI Q45+EDAX Octane Prime, Hillsboro, OR, USA). These samples were placed on aluminum foil sheets for the above EDX analysis.

X-ray photoelectron spectroscopy (XPS) with Al K $\alpha$  radiation (Thermo Fisher Scientific, ESCALAB250Xi, Waltham, MA, USA) was employed to investigate the surface chemistry properties. All the binding energies were calibrated by using the contaminant carbon (C 1s  $\frac{1}{4}$  284.8 eV) as a reference.

The specific surface areas and distribution of pore size were analyzed by Brunauer–Emmett–Teller (BET) and Barrett–Joyner–Halenda (BJH) methods using the N<sub>2</sub> adsorption-desorption curves (Micromeritics ASAP 2460, Shanghai, China).

The Electron paramagnetic resonance (EPR/ESR) experiments were determined by electron spin resonance spectroscopy (Bruker E500, Berlin, German) using DMPO capture agent, in which the samples were in a 40 mM DMPO solution with aqueous dispersion for DMPO–•OH and methanol dispersion for DMPO–•O<sub>2</sub><sup>•−</sup>.

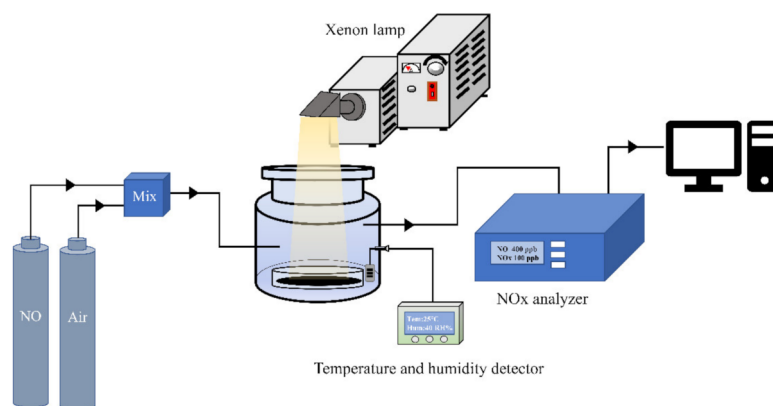
The photoelectrochemical (PEC) measurements were performed with a CHI660E electrochemical workstation (Chenhua Instruments, Inc., Shanghai, China) using aqueous 5 mol·L<sup>−1</sup> Na<sub>2</sub>SO<sub>4</sub> as the electrolyte. 300 W Xenon lamp equipped with a UV cutoff filter ( $\lambda \geq 420$  nm) was used as a light source. Standard calomel electrode (SCE) was employed as the reference electrode and Pt slice as the counter electrode. The working electrode was an indium tin oxide (ITO, 20 × 20 × 1.1 mm, 15  $\Omega$ , Sigma-Aldrich Co., St. Louis, MO, USA) glass coated with the prepared samples. Electrochemical impedance spectroscopy (EIS) was recorded in the frequency range of 0.01–100,000 Hz with a sine wave of 5 mV.

Photoluminescence (PL) analyses were performed using a Raman-Transient Fluorescence Spectrometer equipped with Laser Raman Focused Fiber (LabRAM HR Evolution, Horiba France S.A.S Co. Longjumeau, France) at room temperature with excitation at a wavelength of 325 nm. Fluorescence lifetime was measured using an FS5 spectrofluorometer (Edinburgh, 141UK, Livingston, United Kingdom) under excitation at a wavelength of 300 nm.

The in situ Fourier-transform infrared (in situ FT-IR) spectra were recorded on a FT-IR spectrometer (Bruker Vertex 70 FT-IR, Karlsruhe, German) equipped with in situ reaction chamber.

The visible-light photocatalytic activity was evaluated by comparing the effect of NO removal in a continuous-flow reactor at ambient temperature. The volume of the cylindrical reactor is 500 mL. A 300 W commercial xenon lamp equipped with a 420 nm cut-off filter is used as the light source. To monitor and control the humidity of the reaction gas stream, the reaction system is equipped with a humidity detector and a humidifier. Firstly, 50 mg of as-prepared samples and 10 mL of anhydrous ethanol were added to glass dishes, with a diameter of 60 mm, then ultrasonic mixing for 10 min. Uniform sample films were obtained by drying the above suspension at 60 °C in an oven (Figure S1). Lastly, the films were placed in the reactor equipped with a moisture detector and a humidifier. The dry air and NO gases were introduced into the reactor with an initial concentration of about 800 ppb, in which the air and NO flow rates were controlled at 289 mL·min<sup>−1</sup> and 12.98 mL·min<sup>−1</sup> respectively. The reactions were carried out in the dark until the adsorption-desorption equilibrium was reached. The concentrations of NO, NO<sub>2</sub>, and NO<sub>x</sub> (NO<sub>x</sub> represents NO + NO<sub>2</sub>) were monitored using a NO<sub>x</sub> analyzer (Thermo Environmental Instruments Inc., model 42i-TL, Waltham, MA, USA). The experimental setup for photocatalytic NO removal is displayed in Scheme 1. The photocatalytic efficiency  $\eta$  of the samples was calculated as  $\eta = \frac{C}{C_0} \times 100\%$ , where C and C<sub>0</sub> correspond to the concentrations of NO in the outlet and inlet stream, respectively. The concentration of NO<sub>2</sub>, a toxic byproduct of NO conversion,

was calculated according to as  $C_{NO_2} (ppb) = C_{NO_x} - C_{NO}$ , where  $C_{NO_x}$  and  $C_{NO}$  stand for the concentrations of  $NO_x$  and  $NO$  in the outlet, respectively.



**Scheme 1.** Experimental setup for photocatalytic NO removal with real-time monitoring and testing.

### 3.4. Trapping Test

KI and  $KBrO_3$  were used as effective scavengers of  $h^+$  and  $e^-$ , respectively. TEMPO was used as a scavenger for hydroxyl radicals ( $\bullet OH$ ) and singlet molecular oxygen ( $^1O_2$ ), and NA was used as a scavenger for singlet molecular oxygen ( $^1O_2$ ). PBQ was used to scavenge superoxide radicals ( $\bullet O_2^-$ ) [25]. Photocatalysts (50 mg) containing different trapping agents (1 mmol) were dispersed in deionized water (10 mL) and evenly mixed using ultrasonication. These mixed suspensions were evaporated at 60 °C in an oven to form a uniform film. The photocatalytic activity of these different samples was evaluated by the photocatalytic reaction system mentioned above.

## 4. Conclusions

In conclusion,  $Bi@Ba_2TiO_4/BaBi_4Ti_4O_{15}$  nanocomposites were successfully fabricated by a one-step hydrothermal method. The addition of AA causes the reduction of Bi atoms in  $Ba_2TiO_4/BaBi_4Ti_4O_{15}$ , which could form the SPR effect and OVs. The series of characterizations indicate that the OVs and the SPR effect of  $Bi^0$  in  $Bi@Ba_2TiO_4/BaBi_4Ti_4O_{15}$  photocatalyst effectively increase the light absorption capacity, specific surface areas, and separation efficiency of the photogenerated carriers, thus improving its photocatalysis. As a result,  $Ba_2TiO_4/BaBi_4Ti_4O_{15}$  with addition of 0.1 g AA exhibits the best photocatalytic performance with NO removal efficiency of 67.88%, which is 2.6 times that of the  $Ba_2TiO_4/BaBi_4Ti_4O_{15}$ , and the production of the toxic byproduct  $NO_2$  is reduced by 92.02% under the same conditions. Moreover, ambient humidity has little effect on the photocatalytic performance of the  $Bi@Ba_2TiO_4/BaBi_4Ti_4O_{15}$ , and the photocatalyst exhibits excellent reusability after repeated cleaning with deionized water. More importantly, the results of in situ DRIFTS indicate that the main photocatalytic process of NO removal over the  $Bi@Ba_2TiO_4/BaBi_4Ti_4O_{15}$  nanocomposite occurs via an oxidation route, i.e., NO is converted into  $NO_3^-$ . Mechanistic analysis indicates that  $^1O_2$  and photo-generated holes ( $h^+$ ) play a vital role in NO removal. This study demonstrates that the activity  $Bi@Ba_2TiO_4/BaBi_4Ti_4O_{15}$  is barely affected by ambient humidity which is a promising photocatalyst for NO removal.

**Supplementary Materials:** The following supporting information can be downloaded at: <https://www.mdpi.com/article/10.3390/catal12111455/s1>, Figure S1: The optical images of (a) BT/BBT and (b) BT/BBT-0.1 uniform films, Figure S2: Morphology of BT/BBT-0.1 composite: (a) SEM images, (b) element overlay images, elemental mapping of (c) Bi element, (d) Ba element, (e) Ti element, and (f) O element, and (h) EDX images.

**Author Contributions:** Conceptualization, T.G., K.Z. and Q.Z.; investigation, T.G., H.W., W.Z. and J.L. (Jingqi Lin); methodology, T.G., K.Z. and Q.Z.; project administration, K.Z.; visualization, T.G. and J.L. (Jiangyushan Liang); writing—original draft, T.G., K.Z. and C.W.; writing—review and editing, T.G., K.Z., Q.T., A.A.A., J.S.A., P.K.J.R. and C.W. All authors have read and agreed to the published version of the manuscript.

**Funding:** This project was funded by the National Natural Science Foundation of China (Nos. 21976116, 52161145409), Shaanxi Science and Technology Program (No. 2020KWZ-005), SAFEA of China (High-end Foreign Expert Project), and Alexander-von-Humboldt Foundation of Germany (Group-Linkage Program).

**Data Availability Statement:** Not applicable.

**Acknowledgments:** The authors acknowledge Researchers Supporting Project number (RSP-2021/149), King Saud University, Riyadh, Saudi Arabia.

**Conflicts of Interest:** On behalf of all authors, the corresponding author states that there is no conflict of interest.

## References

1. Ovcharov, M.L.; Granchak, V.M. Photocatalytic Conversion of Nitrogen Oxides: Current State and Perspectives: A Review. *Theor. Exp. Chem.* **2021**, *57*, 30–63. [[CrossRef](#)]
2. Jia, Y.; Li, S.; Gao, J.; Zhu, G.; Zhang, F.; Shi, X.; Huang, Y.; Liu, C. Highly efficient (BiO)<sub>2</sub>CO<sub>3</sub>-BiO<sub>2-x</sub>-graphene photocatalysts: Z-Scheme photocatalytic mechanism for their enhanced photocatalytic removal of NO. *Appl. Catal. B Environ.* **2019**, *240*, 241–252. [[CrossRef](#)]
3. Khanal, V.; Balayeva, N.O.; Günnemann, C.; Mamiyev, Z.; Dillert, R.; Bahnemann, D.W.; Subramanian, V. Photocatalytic NO<sub>x</sub> removal using tantalum oxide nanoparticles: A benign pathway. *Appl. Catal. B-Environ.* **2021**, *291*, 119974. [[CrossRef](#)]
4. Lu, Y.; Huang, Y.; Zhang, Y.; Huang, T.; Li, H.; Cao, J.-J.; Ho, W. Effects of H<sub>2</sub>O<sub>2</sub> generation over visible light-responsive Bi/Bi<sub>2</sub>O<sub>2-x</sub>CO<sub>3</sub> nanosheets on their photocatalytic NO<sub>x</sub> removal performance. *Chem. Eng. J.* **2019**, *363*, 374–382. [[CrossRef](#)]
5. Li, X.; Dong, G.; Guo, F.; Zhu, P.; Huang, Y.; Wang, C. Enhancement of photocatalytic NO removal activity of g-C<sub>3</sub>N<sub>4</sub> by modification with illite particles. *Environ. Sci.-Nano* **2020**, *7*, 1990–1998. [[CrossRef](#)]
6. Pan, B.; Wu, Y.; Rhimi, B.; Qin, J.; Huang, Y.; Yuan, M.; Wang, C. Oxygen-doping of ZnIn<sub>2</sub>S<sub>4</sub> nanosheets towards boosted photocatalytic CO<sub>2</sub> reduction. *J. Energy Chem.* **2021**, *57*, 1–9. [[CrossRef](#)]
7. Zhang, K.; Fujitsuka, M.; Du, Y.; Majima, T. 2D/2D Heterostructured CdS/WS<sub>2</sub> with Efficient Charge Separation Improving H<sub>2</sub> Evolution under Visible Light Irradiation. *ACS Appl. Mater. Interfaces* **2018**, *10*, 20458–20466. [[CrossRef](#)]
8. Zhu, Q.; Dar, A.A.; Zhou, Y.; Zhang, K.; Qin, J.; Pan, B.; Lin, J.; Patrocínio, A.O.T.; Wang, C. Oxygen Vacancies Promoted Piezoelectricity toward Piezo-Photocatalytic Decomposition of Tetracycline over SrBi<sub>4</sub>Ti<sub>4</sub>O<sub>15</sub>. *ACS ES&T Eng.* **2022**, *2*, 1365–1375. [[CrossRef](#)]
9. Singh, S.; Kumar, A.; Pandey, S.K.; Singh, D.K.; Kumar, V.; Verma, M.K.; Gupta, A.; Tiwary, D.; Mandal, K. Facile synthesis of efficient heterogeneous photocatalytic and highly dielectric Bi<sub>4</sub>BaTi<sub>4</sub>O<sub>15</sub> ceramic with remarkable applicability in the degradation of rhodamine B dye. *Mater. Technol.* **2021**, *37*, 880–896. [[CrossRef](#)]
10. Du, Y.; Ai, X.; Li, Z.; Sun, T.; Huang, Y.; Zeng, X.; Chen, X.; Rao, F.; Wang, F. Visible-to-Ultraviolet Light Conversion: Materials and Applications. *Adv. Photonics Res.* **2021**, *2*, 2000213. [[CrossRef](#)]
11. Qi, W.; Wang, Y.; Wu, J.; Hu, Z.; Jia, C.; Zhang, H. Relaxor ferroelectric and photocatalytic properties of BaBi<sub>4</sub>Ti<sub>4</sub>O<sub>15</sub>. *Adv. Appl. Ceram.* **2019**, *118*, 418–424. [[CrossRef](#)]
12. Pan, Y.; Chen, S.; Wang, P.; Li, Y.; Zheng, Q. Ge-vacancy improved the optical and electronic properties of GeAs<sub>2</sub> semiconductor. *Ceram. Int.* **2019**, *45*, 19534–19537. [[CrossRef](#)]
13. Fang, H.-X.; Guo, H.; Niu, C.-G.; Liang, C.; Huang, D.-W.; Tang, N.; Liu, H.-Y.; Yang, Y.-Y.; Li, L. Hollow tubular graphitic carbon nitride catalyst with adjustable nitrogen vacancy: Enhanced optical absorption and carrier separation for improving photocatalytic activity. *Chem. Eng. J.* **2020**, *402*, 126185. [[CrossRef](#)]
14. Liu, G.; Huang, Y.; Lv, H.; Wang, H.; Zeng, Y.; Yuan, M.; Meng, Q.; Wang, C. Confining single-atom Pd on g-C<sub>3</sub>N<sub>4</sub> with carbon vacancies towards enhanced photocatalytic NO conversion. *Appl. Catal. B-Environ.* **2021**, *284*, 119683. [[CrossRef](#)]
15. Liu, J.; Bunes, B.R.; Zang, L.; Wang, C. Supported single-atom catalysts: Synthesis, characterization, properties, and applications. *Environ. Chem. Lett.* **2018**, *16*, 477–505. [[CrossRef](#)]
16. Altass, H.M.; Morad, M.; Khder, A.E.-R.S.; Mannaa, M.A.; Jassas, R.S.; Alsimaree, A.A.; Ahmed, S.A.; Salama, R.S. Enhanced Catalytic Activity for CO Oxidation by Highly Active Pd Nanoparticles Supported on Reduced Graphene Oxide /Copper Metal Organic Framework. *J. Taiwan Inst. Chem. Eng.* **2021**, *128*, 194–208. [[CrossRef](#)]
17. Sun, D.; Huang, L.; Li, L.; Yu, Y.; Du, G.; Xu, B. Plasma enhanced Bi/Bi<sub>2</sub>O<sub>2</sub>CO<sub>3</sub> heterojunction photocatalyst via a novel in-situ method. *J. Colloid Interface Sci.* **2020**, *571*, 80–89. [[CrossRef](#)]
18. Yang, G.; Liang, Y.; Wang, K.; Yang, J.; Zeng, Z.; Xu, R.; Xie, X. Simultaneous introduction of 0D Bi nanodots and oxygen vacancies onto 1D Bi<sub>6</sub>Mo<sub>2</sub>O<sub>15</sub> sub-microwires for synergistically enhanced photocatalysis. *Chem. Eng. J.* **2021**, *409*, 128098. [[CrossRef](#)]

19. Li, J.; Zhang, W.; Ran, M.; Sun, Y.; Huang, H.; Dong, F. Synergistic integration of Bi metal and phosphate defects on hexagonal and monoclinic BiPO<sub>4</sub>: Enhanced photocatalysis and reaction mechanism. *Appl. Catal. B-Environ.* **2019**, *243*, 313–321. [[CrossRef](#)]
20. Duan, Y.; Zhang, M.; Wang, L.; Wang, F.; Yang, L.; Li, X.; Wang, C. Plasmonic Ag-TiO<sub>2-x</sub> nanocomposites for the photocatalytic removal of NO under visible light with high selectivity: The role of oxygen vacancies. *Appl. Catal. B Environ.* **2017**, *204*, 67–77. [[CrossRef](#)]
21. Duan, Y.; Luo, J.; Zhou, S.; Mao, X.; Shah, M.W.; Wang, F.; Chen, Z.; Wang, C. TiO<sub>2</sub>-supported Ag nanoclusters with enhanced visible light activity for the photocatalytic removal of NO. *Appl. Catal. B Environ.* **2018**, *234*, 206–212. [[CrossRef](#)]
22. Alshorifi, F.T.; Alswat, A.A.; Salama, R.S. Gold-selenide quantum dots supported onto cesium ferrite nanocomposites for the efficient degradation of rhodamine B. *Heliyon* **2022**, *8*, e09652. [[CrossRef](#)] [[PubMed](#)]
23. Jiang, X.; Ji, Y.; Li, J.; Zhu, Y.; Kang, T.; Zhong, Z.; Su, F.; Xu, G. Impact of oxygen vacancy in CuO-ZnO catalysts on the selectivity of dimethyldichlorosilane monomer in the Rochow reaction. *Mol. Catal.* **2021**, *504*, 111453. [[CrossRef](#)]
24. Mu, F.; Dai, B.; Zhao, W.; Yang, X.; Zhao, X.; Guo, X. In-situ construction of amorphous/crystalline contact Bi<sub>2</sub>S<sub>3</sub>/Bi<sub>4</sub>O<sub>7</sub> heterostructures for enhanced visible-light photocatalysis. *Chin. Chem. Lett.* **2021**, *32*, 2539–2543. [[CrossRef](#)]
25. Shi, M.; Rhimi, B.; Zhang, K.; Xu, J.; Bahnemann, D.W.; Wang, C. Visible light-driven novel Bi<sub>2</sub>Ti<sub>2</sub>O<sub>7</sub>/CaTiO<sub>3</sub> composite photocatalyst with enhanced photocatalytic activity towards NO removal. *Chemosphere* **2021**, *275*, 130083. [[CrossRef](#)]
26. Zhang, W.; Li, S.; Ma, H.; Hu, D.; Kong, X.; Uemura, S.; Kusunose, T.; Feng, Q. Ferroelectric mesocrystalline BaTiO<sub>3</sub>/BaBi<sub>4</sub>Ti<sub>4</sub>O<sub>15</sub> nanocomposite: Formation mechanism, nanostructure, and anomalous ferroelectric response. *Nanoscale* **2019**, *11*, 3837–3846. [[CrossRef](#)]
27. Wu, Y.-C.; Wang, S.-F.; Chen, S.-H. Microstructural Investigation of Ba(Ti<sub>(1-x)</sub>Mn<sub>x</sub>)O<sub>3</sub> Ceramics with 6H- and 12R-Polytypes. *J. Am. Ceram. Soc.* **2009**, *92*, 2099–2108. [[CrossRef](#)]
28. Lv, X.; Zhang, Z.; Cao, Z.; Jiang, W.; Shi, L.; Zhao, X.; Ma, L.; Wang, T.; Peng, S. Bi@Bi<sub>4</sub>Ti<sub>3</sub>O<sub>12</sub>/TiO<sub>2</sub> films on glass with photocatalytic and self-cleaning performance. *J. Am. Ceram. Soc.* **2020**, *103*, 3104–3118. [[CrossRef](#)]
29. Li, T.; Huang, Y.; Ding, K.; Wu, P.; Abbas, S.C.; Ghausi, M.A.; Zhang, T.; Wang, Y. Newly designed PdRuBi/N-Graphene catalysts with synergistic effects for enhanced ethylene glycol electro-oxidation. *Electrochim. Acta* **2016**, *191*, 940–945. [[CrossRef](#)]
30. Jaiswal, S.K.; Kumar, J. On the X-ray photoelectron spectra, oxygen permeability, and electrical conductivity variations in (Ba<sub>0.5</sub>Sr<sub>0.5</sub>)(Zn<sub>η</sub>Fe<sub>1-η</sub>)O<sub>3-η</sub> (η=0, 0.2) system. *Ionics* **2021**, *27*, 1323–1329. [[CrossRef](#)]
31. Li, P.; Guo, X.; Wang, S.; Zang, R.; Li, X.; Man, Z.; Li, P.; Liu, S.; Wu, Y.; Wang, G. Two-dimensional Sb@TiO<sub>2-x</sub> nanoplates as a high-performance anode material for sodium-ion batteries. *J. Mater. Chem. A* **2019**, *7*, 2553–2559. [[CrossRef](#)]
32. Chen, Y.; Li, J.-F.; Liao, P.-Y.; Zeng, Y.-S.; Wang, Z.; Liu, Z.-Q. Cascaded electron transition in CuWO<sub>4</sub>/CdS/CDs heterostructure accelerating charge separation towards enhanced photocatalytic activity. *Chin. Chem. Lett.* **2020**, *31*, 1516–1519. [[CrossRef](#)]
33. Becker, W. Fluorescence lifetime imaging—Techniques and applications. *J. Microsc.* **2012**, *247*, 119–136. [[CrossRef](#)] [[PubMed](#)]
34. Wang, M.; Zheng, W.; Tao, Z.; Zhang, L.; Luan, H.; Sun, X.; Han, J. Enhanced photocatalytic performance of ferroelectric-based SrBi<sub>4</sub>Ti<sub>4</sub>O<sub>15</sub>/SnS<sub>2</sub> hybrids by piezoelectric effect. *J. Alloys Compd.* **2021**, *883*, 160743. [[CrossRef](#)]
35. Li, N.; Shi, M.; Xin, Y.; Zhang, W.; Qin, J.; Zhang, K.; Lv, H.; Yuan, M.; Wang, C. Oxygen vacancies-modified S-scheme Bi<sub>2</sub>Ti<sub>2</sub>O<sub>7</sub>/CaTiO<sub>3</sub> heterojunction for highly efficient photocatalytic NO removal under visible light. *J. Environ. Chem. Eng.* **2022**, *10*, 107420. [[CrossRef](#)]
36. Li, Z.; Yang, W.; Xie, L.; Li, Y.; Liu, Y.; Sun, Y.; Bu, Y.; Mi, X.; Zhan, S.; Hu, W. Prominent role of oxygen vacancy for superoxide radical and hydroxyl radical formation to promote electro-Fenton like reaction by W-doped CeO<sub>2</sub> composites. *Appl. Surf. Sci.* **2021**, *549*, 149262. [[CrossRef](#)]
37. Goebbert, D.J.; Garand, E.; Wende, T.; Bergmann, R.; Meijer, G.; Asmis, K.R.; Neumark, D.M. Infrared Spectroscopy of the Microhydrated Nitrate Ions NO<sub>3</sub><sup>-</sup>(H<sub>2</sub>O)<sub>(1-6)</sub>. *J. Phys. Chem. A* **2009**, *113*, 7584–7592. [[CrossRef](#)]
38. Nguyen, H.P.; Del Valle, S.P.; Marie, O. NO<sub>x</sub> adsorption on K and Ba loaded on zirconia-titania NSR catalysts: A comparative study by in situ and operando IR spectroscopy. *Appl. Catal. B Environ.* **2018**, *231*, 391–399. [[CrossRef](#)]
39. Shen, T.; Shi, X.; Guo, J.; Li, J.; Yuan, S. Photocatalytic removal of NO by light-driven Mn<sub>3</sub>O<sub>4</sub>/BiOCl heterojunction photocatalyst: Optimization and mechanism. *Chem. Eng. J.* **2021**, *408*, 128014. [[CrossRef](#)]
40. Zhao, Q.; Chen, B.; Li, J.; Wang, X.; Crocker, M.; Shi, C. Insights into the structure-activity relationships of highly efficient CoMn oxides for the low temperature NH<sub>3</sub>-SCR of NO<sub>x</sub>. *Appl. Catal. B Environ.* **2020**, *277*, 119215. [[CrossRef](#)]
41. Zhao, S.; Fu, M.; Li, Y.; Hu, X.; Yuan, C.; Pan, R. Facile hydrothermal preparation of a ZnFe<sub>2</sub>O<sub>4</sub>/TiO<sub>2</sub> heterojunction for NO<sub>x</sub> removal. *Mol. Catal.* **2021**, *507*, 111570. [[CrossRef](#)]
42. Shi, X.; Wang, P.; Li, W.; Bai, Y.; Xie, H.; Zhou, Y.; Ye, L. Change in photocatalytic NO removal mechanisms of ultrathin BiOBr/BiOI via NO<sub>3</sub><sup>-</sup> adsorption. *Appl. Catal. B-Environ.* **2019**, *243*, 322–329. [[CrossRef](#)]